Large-Eddy Simulation of Flow over Two-Dimensional Obstacles: High Drag States and Mixing

ERIC D. SKYLLINGSTAD AND HEMANTHA W. WIJESEKERA

College of Oceanic and Atmospheric Sciences, Oregon State University, Corvallis, Oregon

(Manuscript received 8 March 2002, in final form 23 June 2003)

ABSTRACT

A three-dimensional large-eddy simulation (LES) model was used to examine how stratified flow interacts with bottom obstacles in the coastal ocean. Bottom terrain representing a 2D ridge was modeled using a finite-volume approach with ridge height (4.5 m) and width (~30 m) and water depth (~45 m) appropriate for coastal regions. Temperature and salinity profiles representative of coastal conditions giving constant buoyancy frequency were applied with flow velocities between 0.16 and 0.4 m s^{-1}. Simulations using a free-slip lower boundary yielded flow responses ranging from transition flows with relatively high internal wave pressure drag to super-critical flow with relatively small internal wave drag. Cases with high wave drag exhibited strong lee-wave systems with wavelength of ~100 m and regions of turbulent overturning. Application of bottom drag caused a 5–10-m-thick bottom boundary layer to form, which greatly reduced the strength of lee-wave systems in the transition cases. A final simulation with bottom drag, but with a much larger obstacle height (16 m) and width (~400 m), produced a stronger lee-wave response, indicating that large obstacle flow is not influenced as much by bottom roughness. Flow characteristics for the larger obstacle were more similar to hydraulic flow, with lee waves that are relatively short in comparison with the obstacle width. The relatively strong effect of bottom roughness on the small obstacle wave drag suggests that small-scale bottom variations may be ignored in internal wave drag parameterizations. However, the more significant wave drag from larger-scale obstacles must still be considered and may be responsible for mixing and momentum transfer at distances far from the obstacle source.

1. Introduction

A good understanding of boundary layer processes in the ocean is essential for developing an accurate, overall picture of the ocean circulation. This is particularly true in coastal regions where turbulent mixing may be responsible for a significant portion of the ocean vertical buoyancy flux. The relatively shallow depth of the coastal environment forces a unique boundary layer structure where the surface and bottom boundary layers occupy a considerable fraction of the water column. At the bottom, roughness elements can have a pronounced influence on local circulation, forcing internal waves and increased mixing. Coastal bathymetry is often complex, implying that increased turbulence from bottom interaction of mean and tidal currents is a likely process defining the coastal bottom boundary layer.

Recent studies show that coastal flows over isolated bumps or sills can behave much like a hydraulically controlled two-fluid system with jump conditions and elevated turbulence. For example, Farmer and Armi (1999) observed a strong hydraulic undular jump over a sill with accompanying Kelvin–Helmholtz instability and internal wave activity. Nash and Moum (2001, hereinafter NM) observed a similar hydraulic controlled flow over Stonewall Bank off the central Oregon coast, although the bump in this case was considerably broader and less steep than the Farmer and Armi case and the jump did not appear to have trailing lee waves. They point out that very few measurements of mixing have been made in continental shelf regions and that most existing observations have avoided regions of rough bottom topography. In general, observations of boundary layer turbulence in both the ocean and atmosphere are lacking in regions of complex topography. As a consequence, we do not have a strong basic understanding of how turbulent boundary layers interact with obstacles that are of the same order depth as the boundary layer.

Much of our understanding of geophysical flow interaction with orography is based on studies of atmospheric mountain waves where an infinite depth fluid can be assumed and the bottom boundary layer structure is considered of secondary importance (e.g., Peltier and Clark 1979; Durran 1986; Smith 1985). Studies of flow over bottom topography applicable to the ocean are mainly derived from laboratory experiments of either hydraulically controlled fluids or uniformly stratified

Corresponding author address: Dr. Eric D. Skyllingstad, COAS, 104 Ocean Admin. Bldg., Oregon State University, Corvallis, OR 97331.
E-mail: skylling@coas.oregonstate.edu

flow over topography without separation or a fully developed turbulent boundary layer. For example, Baines (1979) presents results from a series of experiments showing how vertical stratification and flow velocity affect the structure of internal waves generated by topography and confined by a rigid lid.

We know from NM and numerous atmospheric studies that bottom obstacles can exert a significant drag on the overlying fluid, far exceeding typical aerodynamic frictional drag from small-scale (<0.1 m) roughness elements. The strength of this drag can vary widely depending on the flow stratification and velocity. Parameterizations of mountain wave drag based mainly on linear internal wave solutions have been implemented in atmospheric models, yielding substantial improvements in the atmospheric general circulation (e.g., Kim and Arakawa 1995). In contrast, present models of the coastal ocean (e.g., Blumberg and Mellor 1987; Allen et al. 1995) only account for bottom roughness through simple drag laws and do not parameterize the effects of subgrid-scale topographic features. This is a consequence of our very limited knowledge of how the bottom boundary layer interacts with terrain variations and how these features affect mixing and momentum exchange in coastal waters. Understanding the role of flow properties in determining topographic drag is an important goal if we are to improve simulations of the ocean circulation.

a. Hydraulic flow

Flow over coastal obstacles is often described in terms of hydraulic flow theory. Single-layer hydraulic flows are characterized using a Froude number defined as $F_h = U/(\sqrt{gD})$, where U is the flow velocity, g is gravity, and D is the flow depth. When F_h is greater than 1 (supercritical) or less than 1 (subcritical) everywhere, the flow behaves symmetrically when passing over an obstacle (Fig. 1). When F_h is slightly subcritical upstream from an obstacle, then the flow becomes "transcritical" and can make a transition from subcritical to supercritical while passing over the obstacle. Transitional flows produce a strong acceleration in the lee of the obstacle and are often turbulent in the downstream supercritical region before returning back to a subcritical state through a hydraulic jump. It is these transitional flows that generate high drag states.

Hydraulic flow behavior normally assumes that the flow is hydrostatic, which is a good approximation for obstacles that have a long horizontal scale such that D/L, where L is the obstacle width, is much less than 1. If, however, D/L approaches 1, then the flow can generate dispersive, nonhydrostatic waves that propagate energy away from the obstacle and modify or prevent the formation of a well-defined hydraulic jump. In general, the focus of this paper is on obstacles with scales for which nonhydrostatic effects are important and result in dispersive internal waves.
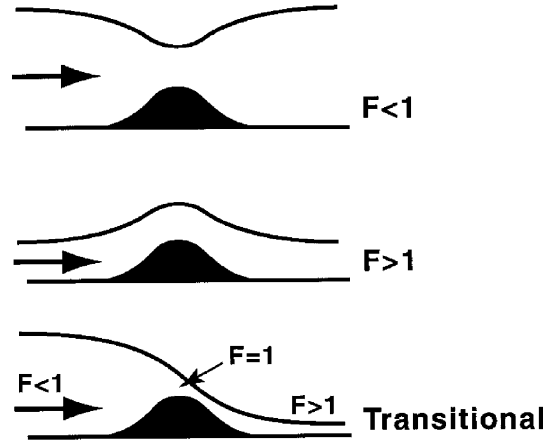

FIG. 1. Schematic showing the response of a one-layer fluid as it passes over a 2D obstacle. The Froude number F is defined in the text.

b. Stratified flow

When flows are uniformly stratified, the hydraulic description is insufficient because of propagating internal waves. Nevertheless, stratified flows can still exhibit transitional behavior if flow parameters are within certain values (e.g., see Durran 1986). In contrast to hydraulic flows that typically generate a distinct jump condition downstream from the obstacle, transition states in uniformly stratified flows are distinguished by an amplified wave system with strong downslope flow on the lee side of the obstacle, overturning, and trailing lee waves if the obstacle width is sufficiently small. Two significant dimensionless parameters for limited depth flow are the mode number,

$$K = DN/(\pi U), \tag{1}$$

and dimensionless obstacle height,

$$\hat{h} = hN/U, \tag{2}$$

where

$$N = \sqrt{-\frac{g}{\rho}\frac{\partial \rho}{\partial z}},$$

h is the height of the obstacle, z is the vertical coordinate, ρ is density, and g is gravitational acceleration (see Turner 1973, p. 33). The mode number K determines the number of vertical wave components contained in a fluid of depth D and is equal to the inverse internal Froude number. The dimensionless obstacle height $\hat{h}$ is a measure of the flow nonlinearity; as $\hat{h}$ increases, the flow becomes more likely to generate overturning internal waves. A third parameter that is important for determining flow behavior is Na/U, where a is a representative half-width scale of the bottom obstacle. Na/U is similar to D/L for the hydraulic system and determines if the flow will produce primarily dispersive, nonhydrostatic waves ($Na/U < 10$) or hydro-

static wave systems confined mostly to the region near the obstacle ($Na/U > 10$).

Long (1955) derived a nonlinear streamfunction equation for the problem of uniform flow over a bump and determined specific vertical modes or wave behavior based on values of K and the relative obstacle height, h/D. These solutions for a nonhydrostatic case were compared against laboratory tank experiments by both Long (1955) and Baines (1979), showing good agreement in both cases. Two basic classes of flows analogous with single-layer hydraulic flow were described in these studies based on the upstream value of K. When $K < 1$ (supercritical), the flow exhibited a symmetric pattern localized over the obstacle, following the supercritical flow schematic shown in Fig. 1. Obstacle effects in this case were minimal, with the average flow conditions showing little change in crossing over the obstacle. For flows with $K > 1$ (subcritical), Long's solutions predicted lee-wave circulations with overturning, indicating turbulence production and momentum flux.

In addition to the value of K, Long found that overturning was dependent on the height of the obstacle. Two critical heights were calculated by Long, one by assuming hydrostatic conditions (large Na/U) and a second by solving Long's equation for various obstacle heights. Solutions directly from Long's equation were found to be more restrictive, for example, predicting breaking for obstacle heights about $0.05D$ higher than the hydrostatic solutions. Long found that as K was increased above ~ 2, values of critical obstacle height, h_{cr}, decreased in both cases, although the internal wave strength was greatly reduced for these higher modes in comparison with the mode-1 wave forced when $1 < K < 2$. Recently, Lamb (1994) performed numerical simulations with small Na/U (i.e., nonhydrostatic) for $1 < K < 2$ and found that h_{cr} were considerably less than those predicted using Long's equation solutions, especially when K approached 2. Lamb also determined that certain stable solutions from Long's model initially exhibited breaking, but eventually reached equilibrium after long time periods. During the initial transient phase, these flows exhibited overturning and regions of turbulence, indicating that short duration flows (e.g., tidal) in the coastal ocean may never reach equilibrium.

c. Objectives

Actual ocean conditions are usually somewhere between the two fluid system described by hydraulic flow theory and the uniformly stratified flow as represented in the Long and Lamb solutions. For example, NM present a series of cross-section plots showing flow behavior that appears to have a two-layer structure, but also exhibits periods of relatively uniform stratification. In each of their plots, microstructure measurements indicate a sharp rise in pycnocline surfaces and an increase in turbulence downstream from the flow obstruction, suggesting a hydraulic jump. The hydraulic jump observed by NM may also be interpreted as the first component of a lee-wave system analogous to the transition conditions described by Long and Lamb. As a complicating factor, the ocean bottom typically has a turbulent boundary layer dependent on the roughness and current velocity. Our understanding of how bottom turbulence interacts with terrain-induced perturbations is an open question that has not been addressed in past studies that typically assume a free-slip bottom boundary.

In this paper we investigate the behavior of flow over a simple, small-scale two-dimensional obstacle using a three-dimensional large-eddy simulation (LES) model that has been modified to include resolved bottom boundary features. We use an LES model so that turbulence generated by overturning lee waves can be more accurately represented and so that a bottom boundary with resolved turbulent eddies can be forced when considering a rough bottom. This is an improvement over past two-dimensional experiments (e.g., Lamb 1994) where three-dimensional turbulent eddies were not resolved and bottom boundary layer formation was not considered. The importance of three-dimensional dynamics is pointed out in Winters and D'Asaro (1994), who show that accurate representation of breaking waves requires a three-dimensional structure because of convectively forced roll circulations in the plane of the two-dimensional waves.

Cases are examined having uniform stratification and background flow velocity with constant K and H, following the previous Long and Lamb experiments. Idealized experiments are performed, examining $O(40 \text{ m})$-wide, two-dimensional topographic features with an emphasis on understanding obstacle-forced pressure drag and turbulence generation by the interaction of a constant flow with topography for typical coastal conditions. Initial conditions are prescribed using typical coastal ocean parameters for temperature, salinity, flow velocity, obstacle height, and water depth, with K set by assigning different constant flow speeds. Cases with dimensionless height above and below the h_{cr} from Long are modeled. In the experiments Na/U is generally $O(1)$, and so dispersive nonhydrostatic waves are produced in the simulations.

The paper is outlined as follows. In section 2 the model is described along with basic initial conditions used in the experiments. Results are presented in section 3, focusing on the role of K and the obstacle height in controlling the flow behavior and on the effects of bottom roughness and boundary layer formation on obstacle flow. Conclusions are presented in section 4.

2. Model description

Simulations of atmospheric mountain waves normally use a nonhydrostatic, Boussinesq model with open boundary conditions and free-slip lower boundary conditions (see, e.g., Durran 1986). Smooth inflow conditions are prescribed without turbulence or horizontal

variations. LES models have only recently been applied to geophysical problems involving topography and have focused almost exclusively on atmospheric conditions. The first of these studies were presented in Krettenauer and Schumann (1992) and Dörnbrack and Schumann (1993) involving convection over wavy terrain. Of principal interest in these simulations was the effect of terrain on surface heating and resulting convection. The surface layer was poorly resolved in these experiments, and shear-dominated, neutrally stable boundary layers could not be accurately simulated. More recently, Gong et al. (1996), Wu and Squires (1998), Brown et al. (2001), and Calhoun and Street (2001) have used LES to examine neutral flow over a sinusoidal ridge, focusing on the generation of turbulence in the immediate region of the orography. Results from these studies compare favorably with laboratory data, indicating that LES can yield an accurate description of the boundary layer interaction with surface obstacles.

In the experiments presented here we are interested in the effects of topographic features that are of the same scale as the ocean bottom boundary layer depth. Consequently, a realistic boundary layer structure is required, including surface drag (via aerodynamic roughness) and turbulence fluxes. Because the topographic scales of interest overlap turbulence eddy scales, we employ a LES model with resolved topography that is set using a finite-element approach similar to Steppler et al. (2002) and Adcroft et al. (1997). The LES model is based on Skyllingstad et al. (1999) with a modified equation of motion using an enstrophy conserving scheme from Tripoli (1992),

$$\frac{\partial u_i}{\partial t} = \varepsilon_{i,j,k} u_i \eta_k - \frac{\partial}{\partial x_i} \text{KE} - \frac{\partial}{\partial x_j} \langle u_i'' u_j'' \rangle - \frac{\partial \tilde{P}}{\partial x_i}$$
$$- \delta_{i3} g \frac{\rho'}{\rho_0} + \gamma \partial^{12} u_i, \qquad (3)$$

where

$$\langle u_i'' u_j'' \rangle = -K_m \left(\frac{\partial u_i}{\partial x_j} + \frac{\partial u_j}{\partial x_i} \right), \qquad \tilde{P} = \frac{P}{\rho_0} + \frac{2}{3} \overline{q^2},$$

$$\eta_k = \zeta_k + f_k, \qquad \zeta_k = \varepsilon_{k,i,j} \left(\frac{\partial u_j}{\partial x_i} \right), \qquad \text{KE} = \frac{1}{2} u_i^2,$$

u_i are the Cartesian velocity components, t is time, g is the acceleration of gravity, δ_{i3} is the Kronecker delta, ρ' is perturbation density, ρ_0 is a constant average density, P is pressure, K_m is the subgrid-scale eddy viscosity, $\overline{q^2}$ is the subgrid-scale turbulent kinetic energy, and $\gamma \partial^{12} u_i$ is a twelfth-order filter with filter coefficient $\gamma = 0.07$ to remove a $2\Delta x$ artifact of the differencing scheme (see Denbo and Skyllingstad 1996). Topography is prescribed by setting velocity components and subgrid-scale fluxes to zero in grid cells that are part of the solid bottom. Grid cells that are intersected by the terrain surface are approximated by finite volumes assuming

the grid cell is partially filled with the terrain surface. The main effect of this assumption is a modification of the divergence operator for the partially filled grid cells to account for the differing volume. A more complete description of the method is presented in the appendix along with a figure showing how the method performs in comparison with an equivalent terrain-following model.

We investigate cases with both free-slip and frictional bottom boundary conditions parameterized using a roughness-length approach. Application of bottom friction in the LES model leads to the formation of a wall-like bottom boundary layer with resolved turbulent eddies and a logarithmic average velocity profile. Our experiments differ from atmospheric studies of mountain lee waves where boundary layer dynamics, if they are present, are parameterized because the horizontal grid spacing is usually much greater than turbulence eddy scales (e.g., Doyle and Durran 2002). Laboratory experiments, while having parameters more similar to oceanographic conditions, are normally too short in duration to develop a fully turbulent boundary layer. For the ocean conditions considered here, the depth of the boundary layer is nearly the same as the topographic feature. Consequently, the turbulent boundary layer has a significant influence on the topographic internal wave structure and resulting wave drag. Unfortunately, because the turbulent boundary layer requires considerable time to evolve, we are restricted to using periodic boundary conditions with the LES model. Use of an open upstream boundary, as commonly applied in previous lee wave studies, would require prescribing a balanced three-dimensional turbulence field involving both momentum and pressure, or use of a very large upstream domain. To minimize the effects of the periodic boundary, we employ a domain size that is ~30 times the obstacle half-width, which reduces the effects of recirculation. Nevertheless, because of the periodic boundaries, our solutions are of an infinite field of widely spaced obstacles, rather than the singular features described in Farmer and Armi (1999) and NM and modeled in Lamb (1994).

Bottom friction is parameterized by substituting the subgrid-scale momentum flux at the lowest model grid point adjacent to bottom topography. We apply a Monin–Obukhov similarity profile in estimating the bottom momentum flux,

$$\langle u_i'' u_3'' \rangle = C_D u_i, \qquad (4)$$

where the drag coefficient,

$$C_D = \left[\frac{\kappa}{\ln(\delta z / z_o)} \right]^2,$$

$\delta z = \frac{1}{2} \Delta z$ or one-half of the vertical grid spacing, $\kappa = 0.4$ is the von Kármán constant, and z_o is the roughness length. In the present application, we do not impose a wind stress or wave parameterization at the model top.
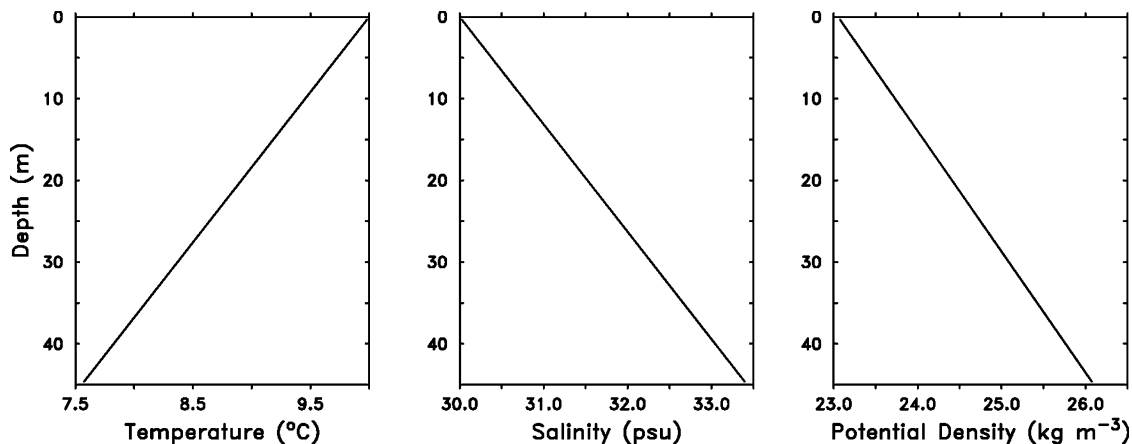
FIG. 2. Initial profiles of temperature, salinity, and potential density yielding $N = 0.025$ s^{-1}.

Bottom orography is set using a ''witch of Agnesi'' profile,

$$h = \frac{h_{max}}{1 + (x/a)^2}, \quad (5)$$

where h_{max} is the maximum height and a is the half-width of the obstacle. Simulations are performed with topography held constant in the y-axis direction and with periodic boundary conditions in the x and y directions. A rectangular channel domain is used with a length of 1200 m (x axis), width of 67.5 m (y axis), depth of 45 m (z axis), and a grid spacing of 0.75 m. Model initial conditions are set using prescribed profiles of temperature and salinity as shown in Fig. 2, with velocity increased linearly from a state of rest to the final value over the first hour of the simulation. Velocity is increased gradually to reduce the formation of transient waves that might form from starting with an impulsive velocity field. The duration of each simulation following the velocity spinup is 3 h for a total simulation time of 4 h.

3. Results

The first question that we wanted to address concerned the behavior of flows with differing values of K. To do this we performed a set of experiments having constant stratification, $N = 0.025$ s^{-1}, and a ridge height of 4.5 m, yielding a range of K similar to values examined in Long (1955) and Lamb (1994). Lower boundary conditions in these experiments were free slip. A

TABLE 1. Parameters for experiments examining transitional flows. Here N in each case is 0.025 s^{-1}; $\hat{h}$ is defined in text.

Case	U (m s^{-1})	K	$\hat{h}$	h_L	h_{hyd}	Na/U
1	0.4	0.89	0.3	NA	NA	0.94
2	0.32	1.12	0.35	5.0 m	3.2 m	1.17
3	0.2	1.79	0.61	9.5 m	7.7 m	1.88
4	0.16	2.24	0.76	3.6 m	2.7 m	2.34

second set of experiments was performed with frictional bottom boundary conditions, using (4) with a roughness length of 0.001 m. We refer to these two sets of experiments as the free-slip and rough-boundary cases, respectively. Obstacle width a in these simulations was set to 15 m.

Flow parameters for each of the basic experiments are shown in Table 1. Values of K for these experiments range from supercritical for case 1 to subcritical for cases 2–4. Critical obstacle heights from Long's equation, h_L, and from Long's equation with the hydrostatic assumption, h_{hyd}, range from above and below the 4.5 obstacle height. Overturning heights given by Long are not based on a witch of Agnesi obstacle profile, but are useful nevertheless in providing a range for comparison. Based on h_L, transition will only occur in case 4, whereas h_{hyd} predicts overturning with cases 2 and 4. We also show values of Na/U, which as mentioned earlier is a measure of the hydrostatic/nonhydrostatic response of the system. For flows examined here, $Na/U \sim O(1)$, indicating that nonhydrostatic, dispersive waves are expected. In general, hydrostatic internal waves are dominant for flows with $Na/U > O(10)$. Our scaled value of a is about 2 times that of Lamb (1994), who considered Na/U between 0.5 and 1.0; however, the obstacle width is still well within the nonhydrostatic limit.

a. Effects of K, free slip

Results from cases 1–4 are presented in Fig. 3, showing vertical–horizontal cross sections of velocity and potential density after 3 hours. In each case, the model spinup generates a series of weak internal waves that propagate downstream from the obstacle and reappear on the left-hand side of the domain after passing through the periodic boundary. These waves appear to have a minimal effect on the upstream conditions, with the strongest lee-wave response evident just downstream from the obstacle. For case 1 ($K = 0.89$), the flow is characterized by an almost symmetric circulation cen-

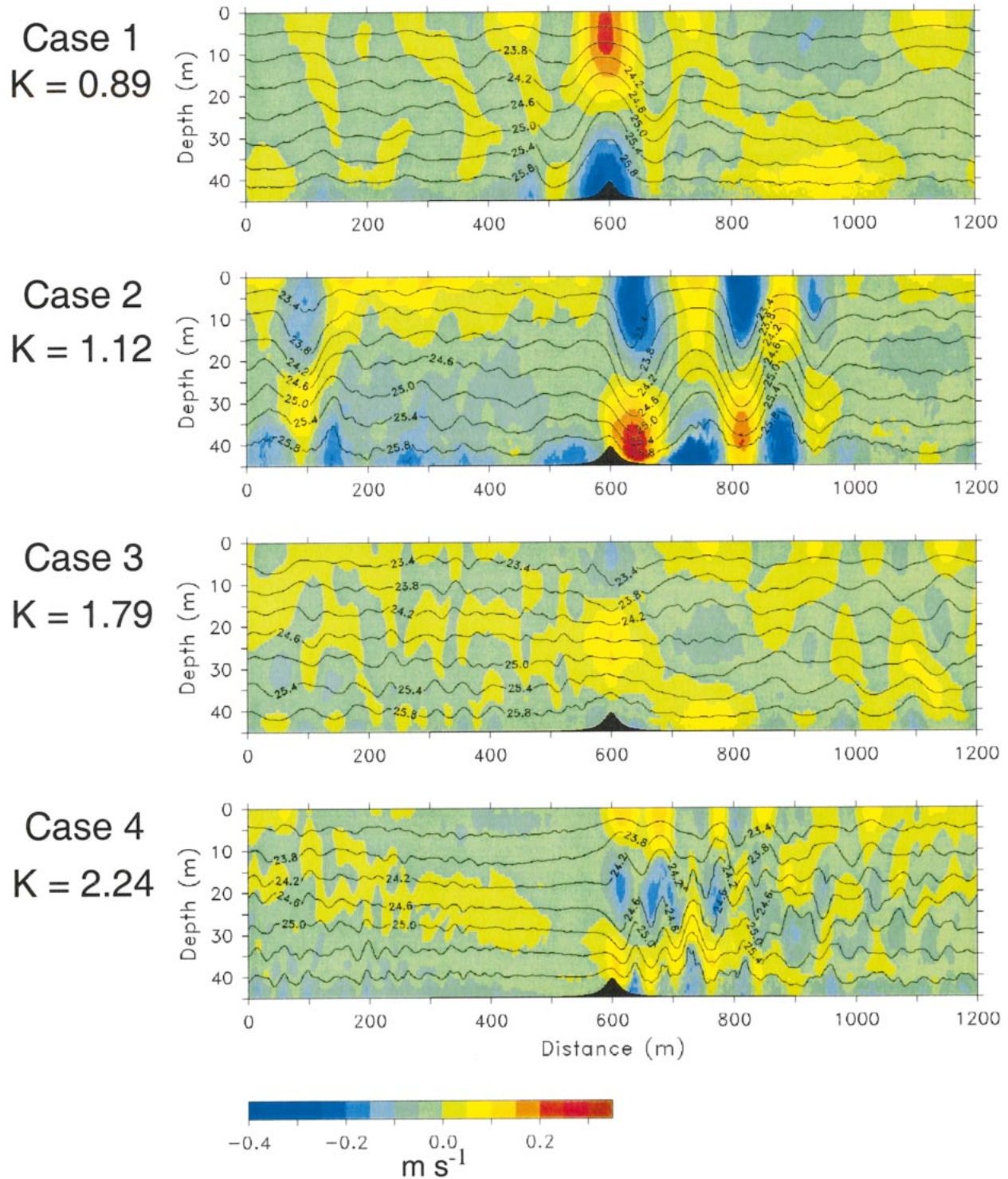FIG. 3. Vertical cross sections of the perturbation horizontal velocity (m s^{-1}) and potential density (kg m^{-3}) taken from $y = 96$ m after 3 h from the free-slip bottom cases 1–4. Perturbation horizontal velocity is calculated by subtracting the initial horizontal velocity.

tered over the obstacle, agreeing with supercritical flow behavior described by Baines (1979). The strongest horizontal velocity perturbation is directly above the ridge with weaker disturbances downstream both at the bottom and top boundary. Potential density tends to behave like streamlines with regions of gradient constriction overlapping areas of high flow speed. Overall, the flow near the ridge is symmetric and does not show a strong transition in crossing over the obstacle.

Increasing K to just above 1 in case 2 ($K = 1.12$) produces a strong lee-wave system consistent with a transition in the flow behavior. Velocity perturbations for this case are much greater than case 1, ranging from 0.1 to 0.7 m s^{-1}, or more than double the inflow velocity magnitude. Vertical displacement of density surfaces show a total range of up to ~15 m or 3 times the obstacle height. Unlike case 1, both the velocity and density fields are asymmetric relative to the ridge axis, with weak flow minima on the upstream side of the ridge and flow maxima just downstream from the obstacle, extending from the top of the obstacle down the entire length of the lee slope. Flow separation, as noted in Farmer and Armi (1999), is not forced in this case. Qualitative comparison of case 2 with Long's solution (Long 1955) and laboratory tank results (e.g., Baines 1979) shows strong similarities. A region of "dead" water is apparent near the model top downstream from the ridge, in roughly the same position as the stagnant zone simulated by Lamb (1994) and observed by Farmer and Armi (1999). High-amplitude lee waves and possible overturning in case 2 are not consistent with the high value of h_L shown in Table 1, although the model obstacle height is greater than h_{hyd} Lamb (1994) notes similar behavior, but for an obstacle with smaller width.

Increasing K further to 1.79 in case 3 leads to the collapse of the transitional flow noted in case 2 and an almost nonexistent lee-wave system. This result is consistent with both h_L and h_{hyd} and numerical results from Lamb (1994) showing that h_{cr} increases as K approaches ~2, preventing wave overturning and transitional flow. Higher-amplitude but shorter-wavelength internal waves reappear when K is increased to 2.24 in case 4. Flow along the lee slope of the obstacle is similar to case 2 with an increased downslope component. However, because of the shorter lee-wave horizontal wavelength, the flow separates about halfway down the slope. Long's solutions predict a reduction in h_{cr} as mode number increases beyond 2, which explains why lee waves are again strong in case 4 and exhibit signs of waves overturning. Reduction in h_{cr} can be thought of as a consequence of the smaller length scales forced by higher mode waves. For example, in Fig. 3 a mode-2 wave is forced, which generates two regions of increased flow above the obstacle, effectively behaving like two wave systems with a vertical scale that is one-half of the fluid depth. Relative to the bottom wave component in the mode-2 solution, the obstacle height appears much taller than in the mode-1 case.

For obstacles with $\hat{h} \ll 1$, linear theory predicts a lee-wave response such that

$$k_j = \frac{\pi}{H}(K^2 - j^2)^{1/2}, \qquad (6)$$

where $k_j = 2\pi/\lambda$ is the horizontal wavenumber, λ is the wavelength, and j is the largest integer less than K (see Baines 1995, p. 263). Equation (6) yields a wavelength of ~180 m for case 2, which is similar to the wave feature shown in Fig. 3. For case 4, (6) predicts a wavelength of ~90 m agreeing with the shorter wavelength produced by the simulation for this case. However, simulated lee waves for case 4 are about 50–60 m long; considerably shorter than the linear prediction. Nonlinear wave steepening and overturning in this case are probably responsible for this disagreement.

b. Perturbation kinetic energy

Figure 3 demonstrates that obstacles can have a large effect on the overall flow depending on the state of the flow and the height of the obstacle. The simulations also suggest that internal wave overturning can generate regions of turbulent mixing that would not otherwise exist if turbulence was limited to just the turbulent bottom boundary layer. Case 4 with free-slip conditions is a particularly interesting simulation because of the generation of overturning in the center of the water column, away from the upper and lower boundaries. Observations of coastal turbulence often show isolated patches of mixing in the stratified pycnocline that are not directly connected with a source region such as the top and bottom boundary layer. Here we present an analysis of the case 4 wave-breaking event shown in Fig. 3, which has similarities to observed pycnocline patches.

Normally, an analysis of turbulence kinetic energy (TKE) could be made from the LES results by subtracting the average current velocity from the full fields to yield a turbulence velocity field (see, e.g., Skyllingstad et al. 1999). In the present case, however, strong velocity perturbations from internal waves exist over much of the domain and do not represent turbulence structures with active mixing. Separating turbulence velocities from internal waves is a difficult task even with balanced three-dimensional fields as produced by the LES model.

A proxy for turbulence strength can be calculated by assuming that cross-stream averages describe both the mean current and velocities associated with internal waves. Here we refer to cross stream as being the direction parallel to the ridge axis. Examination of horizontal plane sections indicates that flow fields forced by the bottom ridge have very little cross-stream variability except in regions of overturning, for example, near $x =$ ~800, $z =$ ~20 in case 4 from Fig. 3. Computing perturbations of u, v, and w using

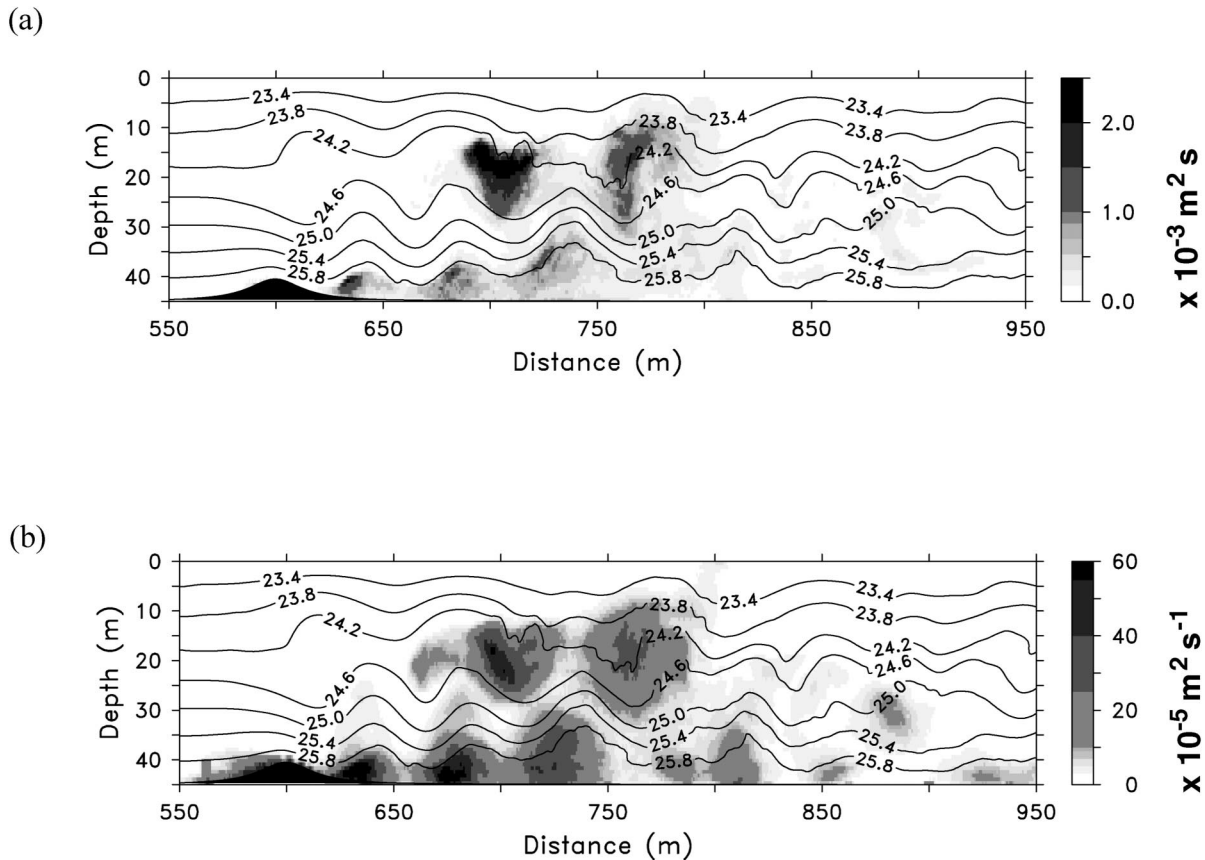$$\hat{u} = u - \frac{1}{L_y} \sum_y u(x, y, z), \qquad (7)$$

(a)

(b)

FIG. 4. Cross-stream averages of (a) estimated TKE and (b) subgrid-scale eddy viscosity K_m from the free-slip bottom case 4 after 3 h. Potential density (km m^{-3}) is also shown to indicate position of the lee-wave system.

where L_y is the number of grid points in the cross-stream direction, yields an estimate of the turbulence kinetic energy, TKE $= \frac{1}{2}(\hat{u}^2 + \hat{v}^2 + \hat{w}^2)$ as shown in Fig. 4a. Also plotted in Fig. 4b is the subgrid-scale eddy viscosity, K_m, which provides an indication of where turbulence is dissipated in the model. Figure 4 shows that turbulence is produced in roughly two vertical patches extending downstream from the obstacle. The first patch is located near the lower boundary with the bottom internal wave system and can be connected with a separation zone that exists behind the obstacle (as shown by the weak current reversal in Fig. 3). A second region of turbulence is present in the middle of the water column about 100 m downstream from the obstacle. Dissipation in this patch appears to be stronger based on the magnitude of K_m. The two patches are separated by a more stratified region created when the flow divides into two modes as it passes over the obstacle.

Horizontal and vertical cross sections taken from a depth of 22 m and near $x = 760$ m (Fig. 5) provide a three-dimensional view of the mixing region. Probably the most obvious feature in Fig. 5a is the lee-wave disturbance that appears as a banded structure extending across the flow. Turbulent motions are superimposed on the wave pattern and generate convergence/divergence

zones in the velocity fields and cross-stream variations in the density field. In the wave troughs (denoted by low density), the velocity field is weak with regions of flow reversal, for example, near $y = 60$ m, $x = 705$ m, and jets, for example, at $y = 35$ m, $x = 755$ m. These circulations are also present in the vertical plane (Fig. 5b) where a number of vortical motions are present, for example, at $y = 46$ m, $z = 22$ m. The vertical cross section also shows that upward motion in the lee wave has large variability in the cross-stream direction, probably because of convectively unstable conditions set up by wave overturning.

c. Frictional drag—Bottom boundary layer formation

Our second set of experiments duplicates the first set, but with prescribed bottom roughness and frictional drag (as discussed in section 2). These cases are referred to as the rough-boundary experiments versus the free-slip cases presented above. Cross-section plots from these experiments are shown in Fig. 6, corresponding respectively to the experiments shown in Fig. 3. It is clear from comparing these two sets of experiments (Figs. 3 and 6) that the bottom boundary layer development has a strong influence on internal wave systems, especially
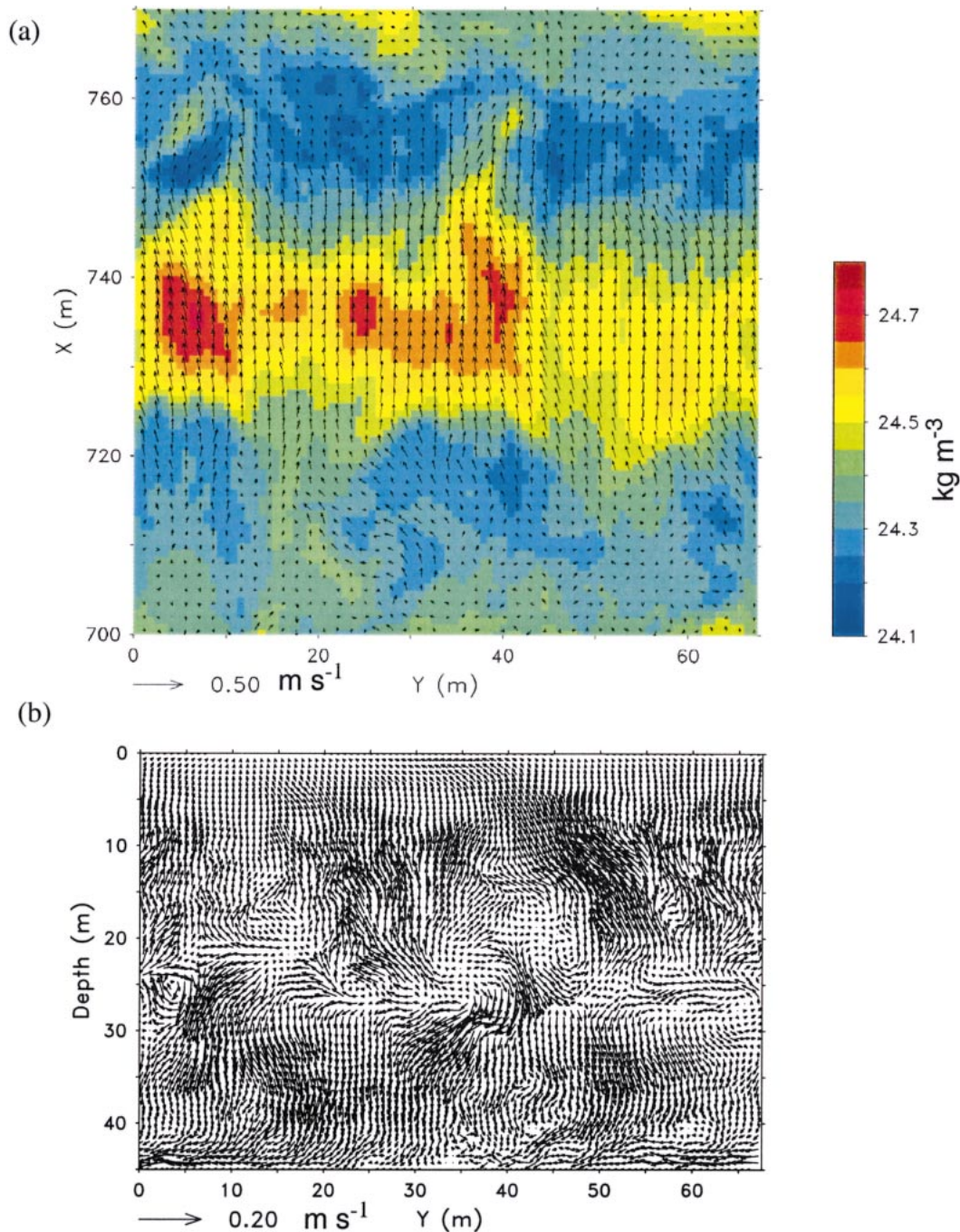
FIG. 5. (a) Horizontal cross section of potential density and horizontal velocity vectors at 22.125-m depth and (b) vertical cross section at $x = 760$ m of velocity vectors at hour 3 from case 4.

when the background current is large (small K). For example, the strong wave system forced in case 2 of the free-slip experiment is much weaker when bottom drag is imposed. Case 1, on the other hand, shows a more significant downstream wave feature that modulates the boundary layer depth, but an overall weaker vertical density surface displacement in comparison with the free-slip simulation.

As the background current is increased, a turbulent boundary layer develops along the model bottom in response to bottom drag. Stronger currents (i.e., smaller K) force more vigorous turbulence because of stronger shear, which leads to a deeper bottom boundary layer. In cases 1 and 2, the bottom boundary layer is deep enough to cause a decrease in the low-level current speed and vertical stratification, which decouples the
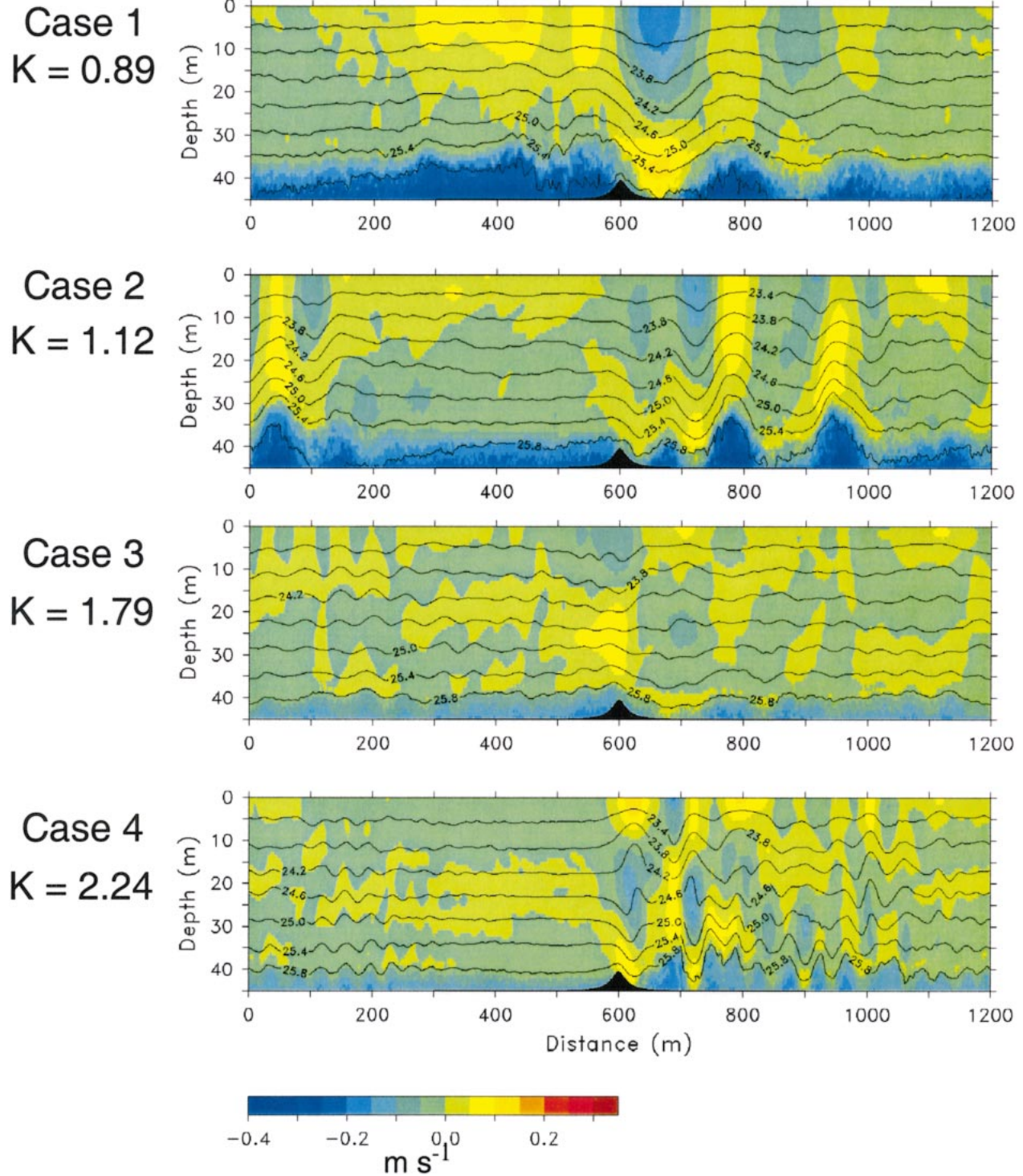
FIG. 6. As in Fig. 3 but from the rough-bottom cases 1–4.

near-bottom flow from the rest of the column. One direct effect of the boundary layer is a reduction in the momentum and energy of the near-bottom mean flow, which decreases the source of energy and momentum for the lee-wave systems. Formation of the bottom boundary layer also reduces the effective height of the obstacle to a level less than h_{cr}, reducing pressure drag and the transition flow structure shown for case 2 in Fig. 3. In addition, reduction in the near-bottom flow speed may also cause the effective K to increase, which
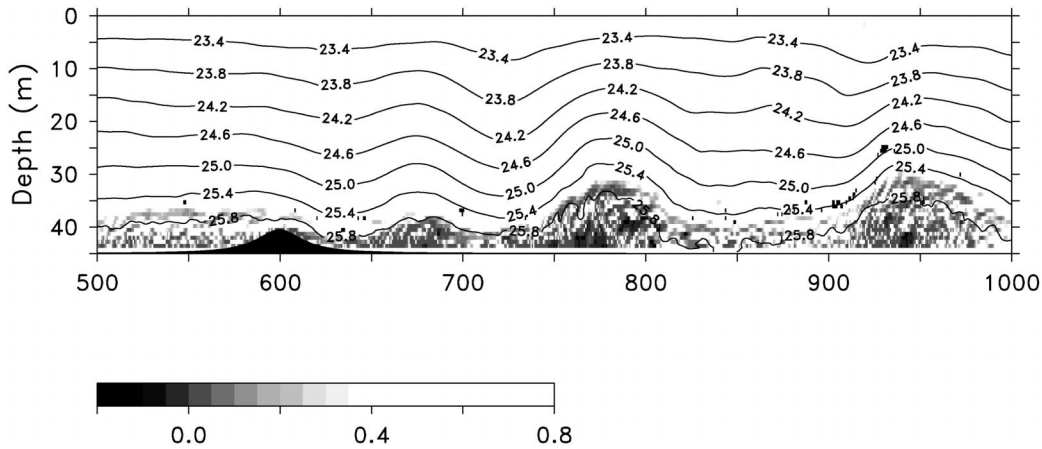
FIG. 7. Horizontal cross section of Ri at hour 3 from case 2 with bottom friction.

corresponds to an increase in h_{cr} and more stringent conditions for flow transition. Because the bottom boundary turbulence strength and layer depth is directly linked to the current speed, the effect of bottom roughness is weaker for the higher mode cases.

Lee waves in case 1 and 2 force changes in the bottom boundary depth downstream from the ridge, resulting in a more vigorous turbulent layer under wave crests in comparison with wave troughs. Stratification in the wave troughs inhibits turbulence, whereas the weaker vertical density gradient in the wave crests enhances turbulence. This is shown by plotting the Richardson number

$$\text{Ri} = N^2 \bigg/ \left(\frac{\partial u_i}{\partial z}\right)^2 \qquad (8)$$

from the rough bottom case 2 (Fig. 7). The formation of waves in these cases is similar to results presented in Uchida and Ohya (2001), who examined how lower boundaries affect lee waves using a two-dimensional direct numerical simulation. They found that strong vortices are produced using both free-slip and no-slip boundary conditions. In our simulations, however, the formation of three-dimensional turbulence limits the strength of recirculation in the lee waves downstream from the obstacle, particularly when bottom friction is applied. Bottom boundary layer formation in cases 3 and 4 also affects internal wave systems as flow velocity is decreased, although to a lessor degree than cases 1 and 2. Weaker mean velocities limit the speed of boundary layer growth, and so the portion of the obstacle above the turbulent boundary layer is greater in comparison with the higher velocity cases.

d. Momentum budget

One of our goals in this study was to examine how obstacles affect ocean currents away from the bottom. To do this we calculated the average velocity at depths between the surface and 37.5 m,

$$u(t) = \frac{1}{n} \sum_{z=0,37.5} u(x, y, z), \qquad (9)$$

where n is the number of grid points. Our intent was to see how internal waves affect momentum above the obstacle, so averaging in the vertical was limited to between 0 and 37.5-m depth, thereby excluding near-bottom blocking and bottom boundary layer formation. Plots of the percentage change in domain-averaged horizontal cross-ridge momentum for the free-slip cases (Fig. 8a),

$$\frac{u(t) - u(t = 1\text{ h})}{u(t = 1\text{ h})} \times 100,$$

show how transition flow in the simulations affects the transfer of momentum to internal waves forced by the obstacle (the initial flow is set to $t = 1$ h because of the 1-h spinup). Without overturning (cases 1 and 3), the average flow decreases by about 2% over the simulation period. In contrast, the transition flow simulated in cases 2 and 4 produces an ~8% decrease in the average velocity by hour 3. Case 2 undergoes an oscillation between 2 and 3 hours where the momentum increases slightly before continuing downward. This behavior is similar to oscillations in the wave drag presented in Lamb (1994) and is discussed in more detail below in our analysis of the momentum budget.

Average flow behavior in the rough bottom cases differs considerably from the free-slip bottom experiments (Fig. 8b). With the exception of case 4, average momentum reduction for these cases is more a function of the initial flow speed, indicating that faster-moving water experiences greater frictional drag and more rapid development of a bottom boundary layer. Reduction in internal wave strength in cases 2 and 4 results in less drag with a rough lower boundary than a free-slip lower boundary. This behavior is similar to the decrease in drag that occurs around spherical objects that have a turbulent boundary layer [e.g., see p. 320–322 from Kundu (1990)]. In the case of spherical objects, the
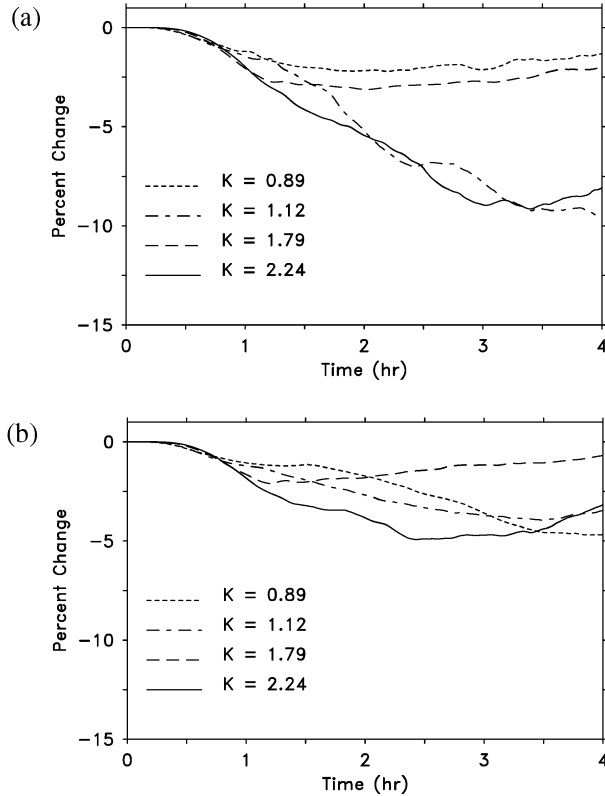
(a)

(b)

FIG. 8. Percentage change in the volume-averaged u component of velocity between the surface and 37.5-m depth for cases 1 ($K =$ 0.89), 2 ($K = 1.12$), 3 ($K = 1.79$), and 4 ($K = 2.24$) with (a) free-slip bottom and (b) rough bottom boundary conditions. Rough bottom has a roughness length of 0.001 m.

formation of a turbulent boundary layer delays the onset of separation, limiting the size of the wake region and the overall form drag. For the obstacle flow studied here, pressure drag is transmitted through internal waves that are forced when flow moves upward over the obstacle. Boundary layer formation reduces the low-level flow speed, thereby limiting the strength of upward motion on the upstream side of the obstacle and related verti- cally propagating internal waves.

Vertical profile plots of the total change in horizon- tally averaged momentum for a given time,

$$\frac{\overline{u}(z, \ t) - \overline{u}(z, \ t = 1 \text{ h})}{\overline{u}(z, \ t = 1 \text{ h})} \times 100,$$

where

$$\overline{u}(z, \ t) = \frac{1}{n_{xy}} \sum_{x,y} u(x, \ y, \ z, \ t), \tag{10}$$

and n_{xy} equals the total number of horizontal grid points excluding topography (Fig. 9), show how the internal wave drag is distributed in the vertical. All cases show the largest decrease in relative velocity near the bottom either from flow blockage (in the free-slip cases) or from bottom drag. In the free-slip cases, the internal wave drag location is dependent on the mode number. For case 2 ($K = 1.12$), drag is maximized in the upper half of the column, whereas case 4 ($K = 2.24$) shows stron- ger drag near the middle of the water column where wave overturning is indicated (see Fig. 3). When bottom friction is applied (Fig. 9b), bottom drag is the dominant momentum loss. However, the importance of form drag is still evident as shown by case 4 ($K = 2.24$) where the flow velocity indicates a small decrease through
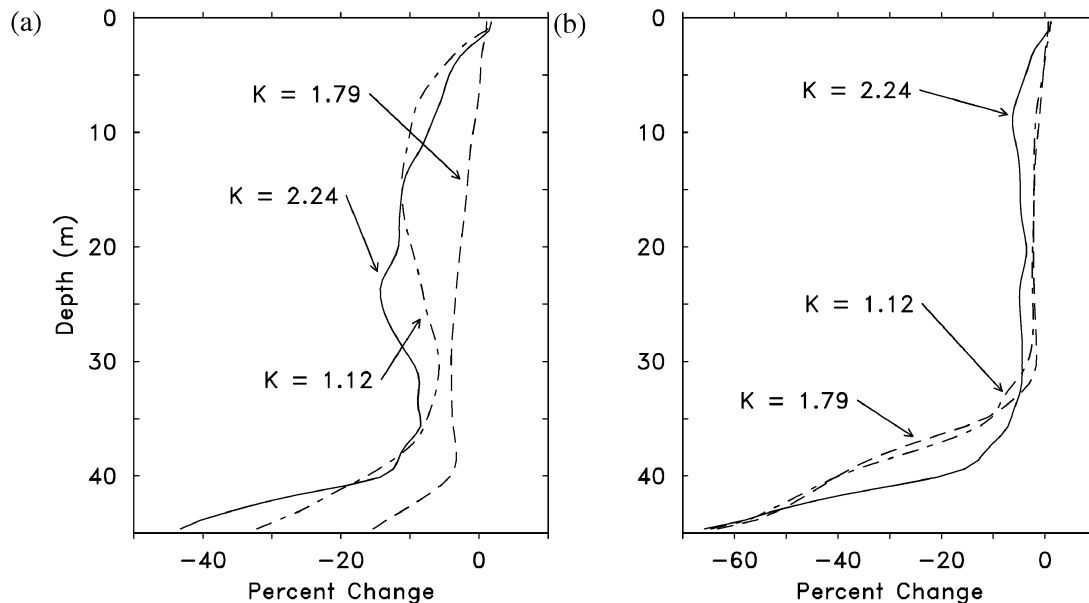
(a)

(b)

FIG. 9. Percentage change in the horizontally averaged u component of velocity at hour 3 for cases 2 ($K = 1.12$), 3 (K = 1.79), and 4 ($K = 2.24$) with (a) free-slip bottom boundary conditions and (b) rough bottom boundary conditions.
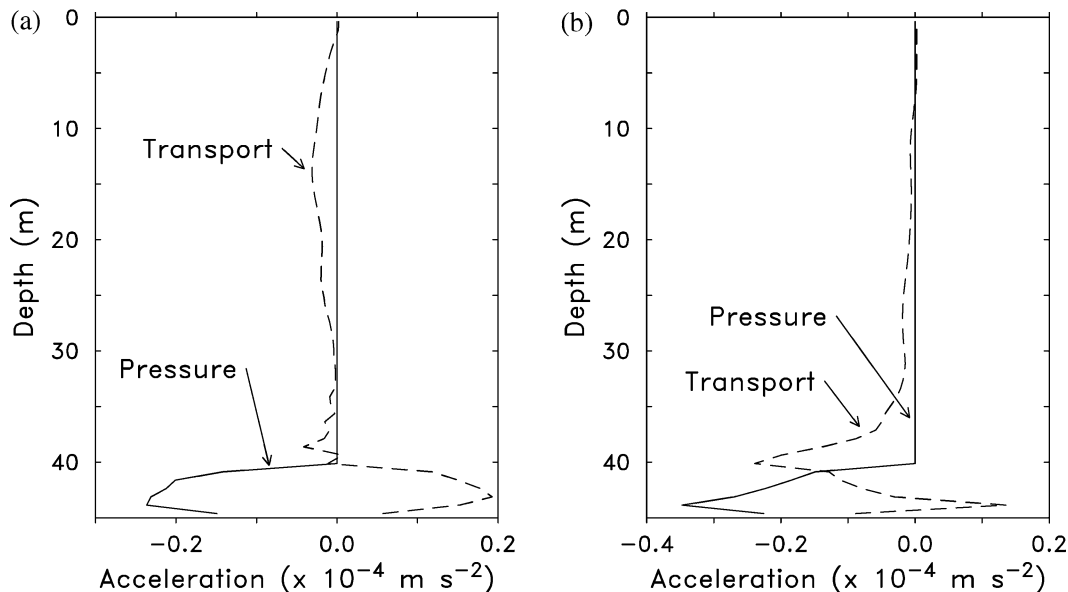
FIG. 10. Horizontally averaged momentum budget terms representing vertical transport, $-\partial(\overline{u'w'} + \overline{\langle u''w''\rangle})/\partial z$, and pressure drag $-\rho^{-1}\partial P/\partial x$ for case 2 with (a) free-slip bottom boundary conditions and (b) rough bottom boundary conditions. Terms are averaged between hours 1 and 2.

most of the water column. In the other cases, drag is much weaker away from the bottom boundary layer in comparison with the free-slip bottom cases.

A better sense of how the obstacle affects the mean flow is revealed by the horizontally averaged momentum budget equation,

$$\frac{\partial \overline{u}}{\partial t} = -\frac{\partial}{\partial z}(\overline{u'w'} + \overline{\langle u''w''\rangle}) - \frac{1}{\rho}\frac{\partial P}{\partial x} + f\overline{v}, \quad (11)$$

where single primes represent departures from the horizontally averaged flow, $\langle u''w''\rangle$ represents the subgrid-scale momentum flux, P is the pressure, f is the Coriolis term, and v is the along-slope velocity. The first term on the right-hand side of (11) represents the vertical divergence of the momentum flux from both resolved-scale and subgrid-scale motions, representing internal waves and turbulence. Bottom friction appears in the subgrid term when it is applied. Except at the surface, term 1 represents the vertical transport of momentum. Term 2 is the horizontal pressure drag induced by the obstacle, and term 3 is the Coriolis force, which is relatively small for the short duration simulations presented here.

Terms 1 and 2, time averaged between hour 1 and 2 for case 2 ($K = 1.12$), are presented in Fig. 10 for both the free-slip and rough bottom cases. These terms are referred to as the transport and pressure terms, respectively, in Fig. 10 (we note that with periodic boundaries the average of the pressure term should equal zero above the obstacle, as is shown in Fig. 10). In the free-slip case, momentum is lost primarily through pressure drag between the bottom and 40-m depth and is redistributed vertically by internal waves. This is shown in Fig. 10a

by a near balance between the low-level pressure term and the transport term below ~40 m. Momentum lost by the pressure term is replaced by momentum transported downward by the internal wave flux. The source of this momentum is the flow above the obstacle height, as shown by the negative transport term between ~40 m and the surface. Turbulence fluxes are also a part of the vertical transport, but have a much weaker influence relative to the internal wave system. Mismatch between pressure drag and vertical transport below 40 m results in a gradual reduction (i.e., negative tendency) in the low-level flow, as shown by the reduced velocity in Fig. 9. In the rough-bottom case, pressure drag is about the same as the free-slip experiment; however, the transport term is negative at the bottom because of bottom drag. Bottom frictional drag in this case is still less in magnitude than the pressure drag, but its effect is compounded because it directly reduces the flow velocity in the boundary layer, which in turn greatly decreases the flux of momentum through vertical internal wave propagation. Momentum transport in the rough case falls off rapidly above the obstacle height, showing almost no influence above ~20 m.

Internal wave momentum transport from case 2 with free-slip conditions as measured by $\overline{u'w'}$ (Fig. 11a) is consistent with mean flow behavior, showing a reversal in sign at about hour 2 and hour 3 and a switch from net positive vertical flux divergence (flow deceleration) to negative vertical divergence (flow acceleration). Variations in $\overline{u'w'}$ also follow the average pressure drag term defined as

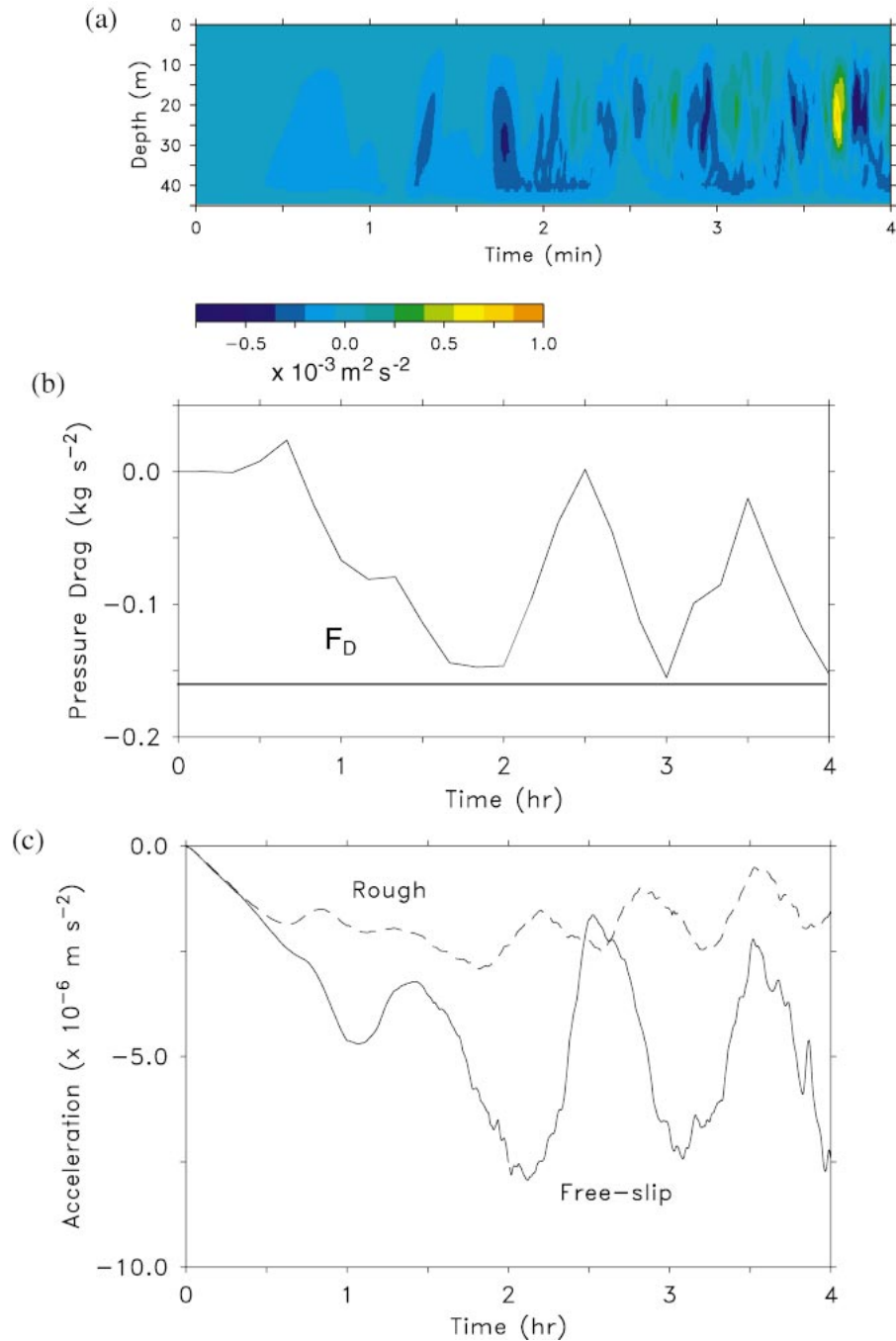$$D_f = \int h(x)\frac{\partial}{\partial x}\overline{P}(z = h) \, dx, \quad (12)$$

FIG. 11. Time series of (a) horizontally averaged momentum flux $\overline{u'w'}$, (b) surface pressure drag, and (c) domain-averaged pressure acceleration term for the free-slip bottom case. Also shown is the acceleration term for the rough bottom case. Horizontal line in (b) represents pressure drag from the analytical linear (F_D) formula given in Baines (1995).

shown in Fig. 11b. Likewise, the average pressure acceleration, defined as the domain average of term 2 in (11), shows a reduction in strength at about 2 and 3 h (Fig. 11c). Also shown in Fig. 11c is the pressure term from the rough case, which is much weaker in comparison with the free-slip result, again showing the pro-

nounced effect of the frictional drag. An estimate of obstacle drag from linear theory for an unbounded fluid (see Baines 1995, p. 245),

$$F_D = \frac{\pi}{8}\rho_o N h^2 \qquad (13)$$

yields a drag value of ~0.16 (shown as a horizontal line in Fig. 11b), which is near the maximum pressure drag produced in the simulation. The similarity between the analytical drag diagnosed from (13) and the value produced in our periodic, limited-depth fluid is of interest because it suggests that transition modes may have an upper-limit drag that is given by the unbounded fluid value. This correspondence may be important when considering internal wave drag parameterizations, which often rely on analytical results to assess obstacle wave drag profiles.

Oscillations in the pressure drag can be explained by examining the time variation of the lee-wave system. Analysis of the pressure fields from the free-slip case 2 around the time of the first flux reversal (Fig. 12) shows that the lee waves trailing behind the obstacle are not stationary in time. At 140 min, the pressure is lower over the lee side of the obstacle under the trough of the first lee wave. Consequently, the bottom pressure gradient over the terrain is on average negative, which according to (12) will cause a negative form drag and downward wave momentum flux. As the mean flow decreases in response to the wave drag, a component of the lee-wave system begins to propagate upstream at around 145 min. Eventually, the wave overtakes the position of the obstacle at ~150 min and causes the horizontal pressure gradient over the obstacle to relax and reverse direction. While the wave is over the obstacle, the form drag is in the same direction as the flow, causing a slight reduction in the negative momentum carried by the wave and a loss of wave energy. At 155 min, the wave propagating over the obstacle decays, leading to the eventual reestablishment of the lee-wave system.

The pattern of upstream lee wave progression shown in Fig. 12 is similar to results presented in Lamb (1994) that also indicated an oscillatory behavior for wave systems in transition flows. Lamb describes a very similar scenario whereby the lee-wave system propagates upstream, causing a reduction and reversal in the wave drag. Alternatively, oscillatory behavior in our solutions may be a result of the periodic boundaries. However, as Fig. 3 shows, lee waves that recirculate in the model are of small amplitude in comparison with the upstream propagating mode shown in Fig. 12.

4. Summary and discussion

Simulations of uniform, stratified flow over a two-dimensional obstacle were performed using a turbulence-resolving large-eddy simulation model. Initial profiles of temperature and salinity representing typical conditions along the western coast of North America were used so that results could be related to ongoing observational and coastal modeling efforts. Realistic velocities ranging from 0.16 to 0.4 m s^{-1} were considered, yielding flow responses ranging from supercritical flow with relatively minor form drag to transitional flows

having strong lee-wave systems, significant wave drag, and regions of turbulence. We found that free-slip lower boundary conditions generated results qualitatively similar to analytical and laboratory tank experiments presented by Long (1955) and Baines (1979). For example, as the mode number of the flow, K, was increased (decreasing velocity), the velocity and density structure exhibited multiple layers in close agreement with past results. Form drag produced by the obstacle was strongly dependent on the mode number and the relative obstacle height. When the obstacle height was greater than the hydrostatic wave-breaking threshold, wave drag resulted in an ~8% decrease in the average flow momentum over a 2-h period. In contrast, obstacle height below the threshold produced average flow deceleration of only ~2%. Our results were in qualitative agreement with Lamb (1994) in showing that obstacle height breaking thresholds based on Long's equation were too high.

Application of bottom frictional drag based on a roughness length of 0.001 m significantly affected the outcome of the simulations, in some cases greatly decreasing the role of lee waves and accompanying wave drag. Frictional drag caused the formation of shear and the development of a surface turbulent boundary layer. For high flow velocity, the boundary layer was deep enough to encompass much of the obstacle height, limiting the effect of the obstruction on the overlying stratified flow. In particular, the mode-1, high-drag transitional flow (case 2) exhibited a substantial decrease in lee-wave strength and overall wave drag. With the introduction of surface roughness, internal wave pressure drag in case 2 was reduced by as much as ~2/3 relative to the free-slip case.

Two main points can be made as a result of this study. First, our results suggest that bottom features can have a major effect on the momentum budget of the coastal ocean without requiring significant turbulence fluxes. Pressure drag can effectively reduce the average velocity through internal wave propagation with wave dissipation possibly occurring some distance from the source region. One implication of this result is that momentum flux estimates from microstructure measurements in areas of complex bottom bathymetry may be missing a portion of the total flux. A second result from this work concerns the sensitivity of pressure form drag to the strength of the turbulent bottom boundary layer. Bottom drag and the formation of a boundary layer can disrupt lee-wave formation, decreasing form drag, and reducing the overall momentum loss from bottom obstacles. As a consequence, the ocean bottom roughness can be a key parameter for determining the effects of bottom orography on the overall momentum budget.

Our results showing that bottom roughness greatly decreases the pressure drag created by obstacles appear to be in conflict with observations such as those of NM. Their observations frequently show a turbulent boundary layer upstream from the obstacle, which, unlike our results, does not prevent the formation of a transitional
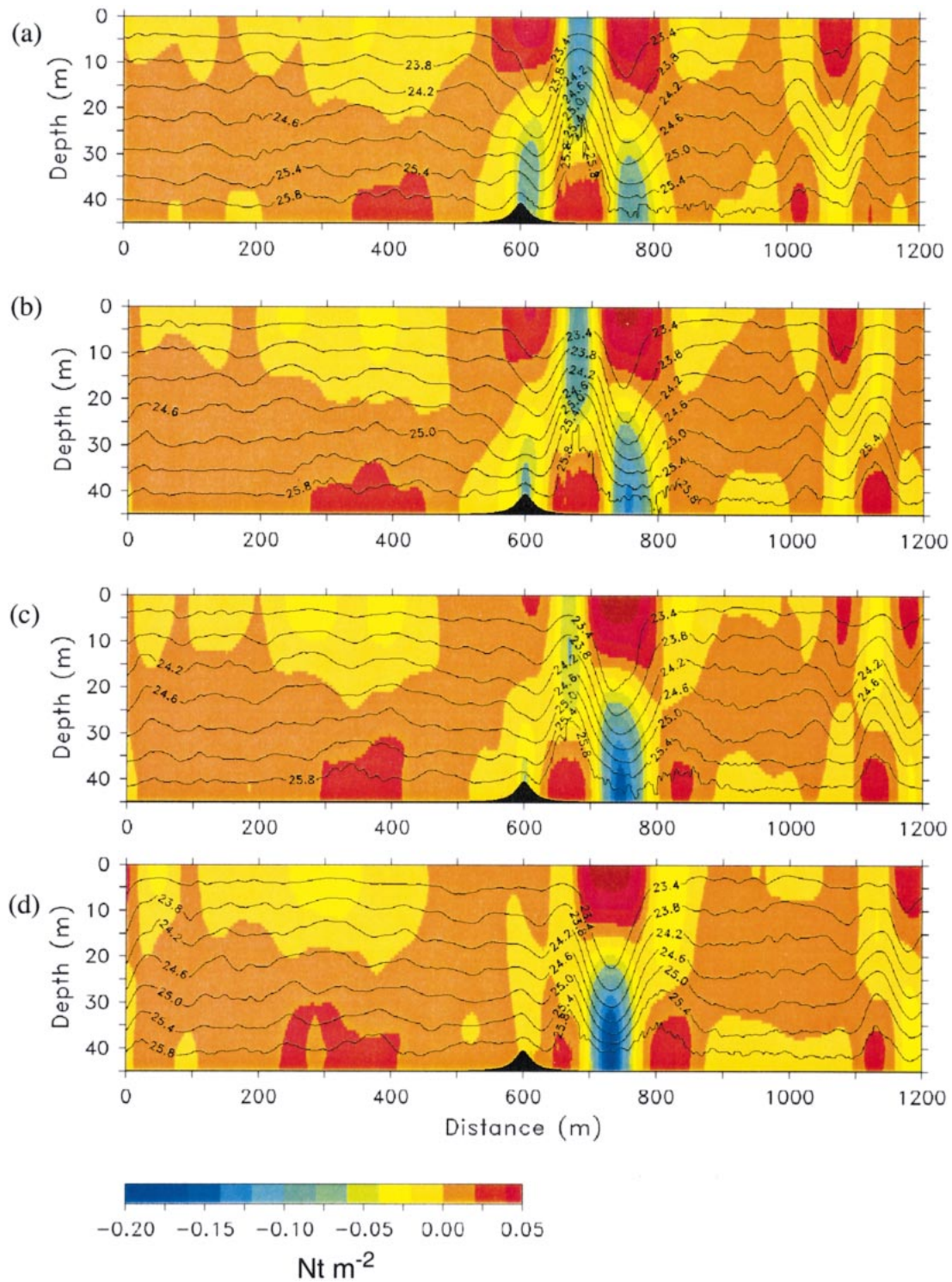
FIG. 12. Horizontal cross sections of pressure (shaded; N m^{-2}) and potential density (contours; kg m^{-3}) taken from $y =$ 48 m at (a) 145, (b) 150, (c) 155, and (d) 160 min of free-slip bottom case 2.
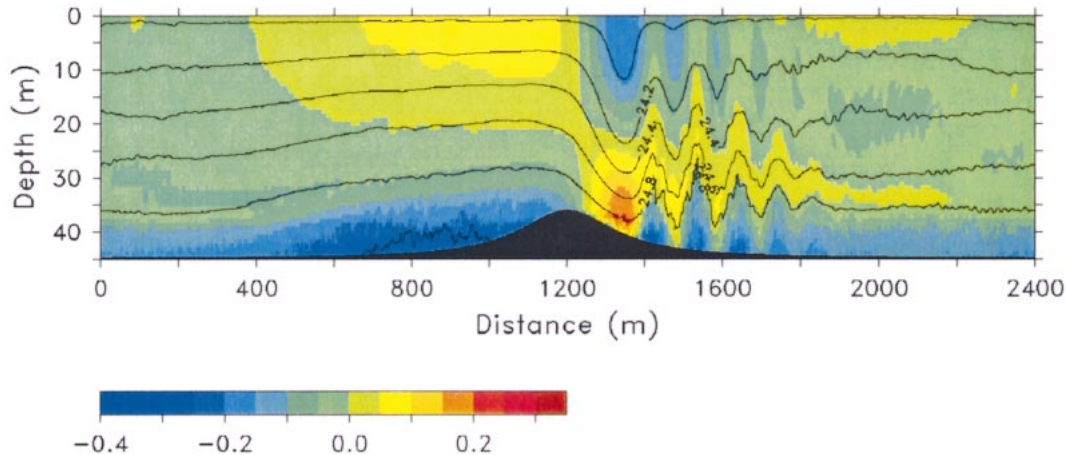
FIG. 13. Vertical cross section of the perturbation horizontal velocity (m s^{-1}) and potential density (kg m^{-3}) taken from $y = 5.6$ m after 3 h for the large domain case. Obstacle half-width in this simulation is 150 m with height of 16 m.

flow. Three main differences between our simulations and the observations from Stonewall Bank are important to note. First, the horizontal scale of Stonewall Bank is roughly 3000 m, versus the $O(100$ m) bump considered here. As a consequence, the flow over Stonewall Bank is well within the hydrostatic range with $Na/U = O(100)$, indicating that obstacle forced waves are non-dispersive and effectively trapped above the obstacle (i.e., weak lee waves). These conditions are more similar to hydraulic flow where flow adjustment occurs through a hydraulic jump rather than through trailing lee waves as produced in our simulations. A second significant difference between our simulations and Stonewall Bank is the scaled height of the obstacle, which yields a value of $hN/U \approx 1$ for Stonewall Bank versus 0.7–0.28 for our cases. Higher values of hN/U promote stronger nonlinear waves, overturning, and turbulence. Last, the conditions observed by NM did not have uniform density gradients or velocity as used in our experiments and there may have been flow features generated by the three-dimensional shape of the bank.

Even with these differences, certain characteristics of the Stonewall Bank flow are in qualitative agreement with our results. For example, NM present three cases having an approximate range of K from ~0.8 to ~3, with one example having K similar to our case 2. For $K \approx 1.5$, they observed a transitional flow that appeared quite sensitive to the flow velocity, ranging from a significant hydraulic jump and turbulence, to relatively smooth flow (when velocities are large) more similar to supercritical conditions. In general, NM found that the strongest transitional flows, as indicated by the integrated turbulence dissipation rates, occurred with K between ~0.8 and 2.0. Nash and Moum (2001) did not find strong evidence for trailing lee waves, which may be a result of the long length scale and hydrostatic nature of the flow, or could be because the waves were too short to be measured accurately using a horizontal profile interval of ~100 m.

At this time, simulating the scales of Stonewall Bank imposes too large of a computational burden for an LES turbulence model as used here. However, as a test we performed an experiment with scales approaching Stonewall Bank by using grid dimensions of 3200 $\times$ 16 $\times$ 150, effectively doubling the along-stream length of the domain (at the cost of marginal cross-stream resolution). We also applied a vertical profile similar to conditions reported in NM, with $N = 0.015$ s^{-1} and $U = 0.2$ m s^{-1}, yielding $K = 1.07$. Obstacle half-width in this case was increased to 200 m, yielding Na/U of 15, which is considerably less than the actual Stonewall Bank value but is large enough to generate a stronger hydrostatic response (see Gallus and Klemp 2000). Obstacle height was increased to 16 m to be consistent with the drop in height for Stonewall Bank shown in NM. A bottom roughness of $z_o = 0.001$ m was applied to see if boundary layer formation affected the flow behavior as in the small-obstacle cases.

A cross section from this case is shown in Fig. 13 after 3 h. Figure 13 shows that the larger-scale obstacle produces a strong downslope flow that ends abruptly in a series of relatively short wavelength lee waves. Overall, Fig. 13 indicates that bottom roughness has little impact on the formation of a strong transition flow for a sufficiently large obstacle, suggesting that our earlier results may not apply to obstacle scales that produce a mainly hydrostatic response. As compared with the small-bump cases, the behavior of this flow is more similar to the observations of NM, although lee waves are still generated in the simulation probably because of the obstacle width still being about one-quarter of the size of Stonewall Bank. Qualitative comparison of the undular jump in this simulation with observations presented in Farmer and Armi (1999) of flow over a similar size obstacle shows better agreement, although the uniform initial conditions used in the model are much different than the observed layered structure.

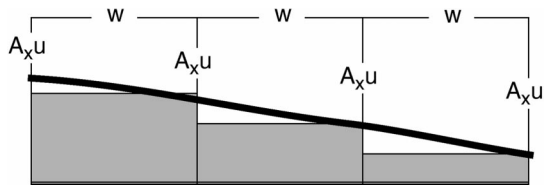Although limited, the experiments performed in this

FIG. A1. Schematic showing finite-volume grid cells adjacent to bottom terrain feature. Heavy line represents the bottom slope. Stippled regions are the portion of the grid cells that are below the bottom and excluded from the model momentum and mass balance. Symbols are explained in the text.

study hint that parameterizing the effects of orography should be possible by exploiting the dependence of wave drag on the internal mode number $DN/\pi U$, relative obstacle height, and obstacle horizontal scale. An approach could be developed following Kim and Arakawa (1995), who consider momentum flux from wave breaking at both high and low levels in the atmosphere based on a mode number tied to local subgrid-scale terrain. Key to most atmospheric mountain wave drag parameterizations is an accurate description of the surface orography. For the coastal ocean, only sparse datasets exist describing bottom features with dimensions important for wave drag (length scales of 100s to 1000s of meters). Increasing accuracy in bottom bathymetry data should eventually allow for the development of wave drag parameterizations based on local values of the internal mode number and height of the terrain features.

A more difficult issue may be the prediction of the turbulent bottom boundary layer depth and the assignment of accurate roughness lengths for coastal waters. Measurements on the California shelf indicate that the bottom behaves like a hydrodynamically smooth surface and should not be modeled using aerodynamically rough, logarithmic approach (Caldwell and Chriss 1979). Given the possible large effects of the bottom boundary layer on pressure form drag, it is critical that we have a better description of the ocean bottom in all coastal regions and estimates of turbulence produced by orographic features. Future LES experiments using more realistic, three-dimensional bottom orography, different roughness length values, and more complex vertical density structure are also needed to fully explore the effects of bottom variations. Ideally, a parameterization will be developed that only takes into account obstacles that are large enough to be unaffected by bottom boundary layer formation.

APPENDIX

Bottom Terrain Representation

Terrain in the LES model is prescribed using a variation of the finite volume method described in Adcroft et al. (1997) and Steppler et al. (2002). Each bottom grid cell that is intersected by terrain is approximated by a reduced volume, which can be implemented by using a modified divergence operator,

$$\nabla u = \delta(A_x u), \tag{A1}$$

where A_x is the area of the grid cell having velocity u as shown in Fig. A1 and δ represents a finite difference over Δx. The modified divergence is used to compute pressure by applying (A1) to (3), assuming a forward difference in time, and setting the predicted velocity divergence to zero, yielding

$$\delta A_x \frac{\partial \tilde{P}}{\partial x_i} = \text{RHS} - \frac{1}{6}\delta(A_x u_{n-1})/\Delta t, \tag{A2}$$

where RHS represents the right-hand side forcing terms, u_{n-1} represents the velocity from the previous time step, and Δt is the time step. The factor of ⅙ follows from a similar equation form used by Harlow and Welch (1965). Equation (A2) is solved iteratively using a conjugate residual method from Smolarkiewicz and Margolin (1994).

Other modifications to the equations of motion include reducing the vertical grid spacing when computing vertical derivatives for bottom boundary points and modifying the grid cell fluxes following Adcroft et al. (1997). We also set the boundary horizontal vorticity component to zero at the bottom boundary, which is
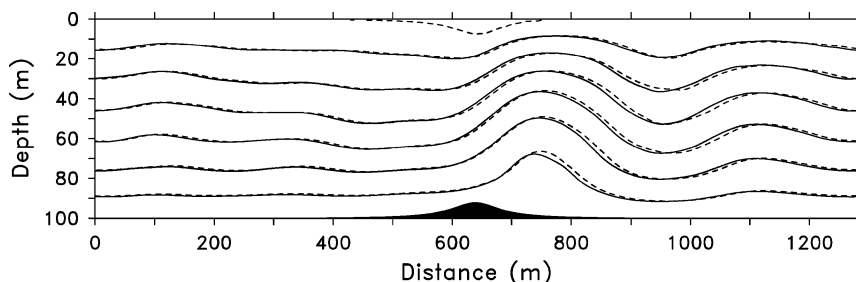

FIG. A2. Contours of potential temperature plotted every 0.5 K from finite-volume (solid) and terrain-following coordinate models after 30 min.

equivalent to prescribing a no-slip bottom boundary condition; bottom drag was introduced explicitly via (4).

Validation of the modified bottom boundary was achieved by performing experiments with a terrain-following coordinate system model having a rigid lid and periodic boundaries, as used in the LES model. The model used in this comparison was the Advanced Regional Prediction System (ARPS) atmospheric model described in Xue et al. (1995). For these comparisons, we used a domain 1280 m in length, 32 m in width, and 100 m deep. Grid resolution in the LES model was set to 2 m in both vertical and horizontal directions, whereas in ARPS we used a horizontal grid spacing of 8 m and a vertical spacing over flat terrain of 2 m. Vertical grid spacing in ARPS over the terrain was allowed to vary by assuming the top of the model was at a constant height of 100 m. Both models were run with $U = 1$ m s^{-1}, $N = 0.035$ s^{-1}, yielding a mode number $K = 1.11$. Obstacle height and half-width were set to 12 and 40 m, respectively, using a witch of Agnesi profile from (5).

A comparison of the two models is presented in Fig. A2 showing potential temperature contours after 30 min. Other than a few minor differences in the position of the lee waves, Fig. A2 shows that the two models produce very similar results, even though they use entirely different numerical techniques.

REFERENCES

Adcroft, A., C. Hill, and J. Marshall, 1997: Representation of topography by shaved cells in a height coordinate ocean model. *Mon. Wea. Rev.,* **125,** 2293–2315.

Allen, J. S., P. A. Newberger, and J. Federiuk, 1995: Upwelling circulation on the Oregon continental shelf. Part I: Response to idealized forcing. *J. Phys. Oceanogr.,* **25,** 1843–1866.

Baines, P. G., 1979: Observations of stratified flow over two-dimensional obstacles in fluid of finite depth. *Tellus,* **31,** 351–371.

——, 1995: *Topographic Effects in Stratified Flows.* Cambridge University Press, 482 pp.

Blumberg, A. F., and G. L. Mellor, 1987: A description of a three-dimensional coastal ocean circulation model. *The Three Dimensional Coastal Ocean Models,* N. S. Heaps, Ed., Coastal and Estuarine Science Series, Vol. 4, Amer. Geophys. Union, 1–16.

Brown, A. R., J. M. Hobson, and N. Wood, 2001: Large-eddy simulation of neutral turbulent flow over rough sinusoidal ridges. *Bound.-Layer Meteor.,* **98,** 411–441.

Caldwell, D. R., and T. M. Chriss, 1979: The viscous sublayer at the sea floor. *Science,* **205,** 1131–1132.

Calhoun, R. J., and R. L. Street, 2001: Turbulent flow over a wavy surface: Stratified case. *J. Geophys. Res.,* **106,** 9295–9310.

Denbo, D. W., and E. D. Skyllingstad, 1996: An ocean large-eddy model with application to deep convection in the Greenland Sea. *J. Geophys. Res.,* **101,** 1095–1110.

Dörnbrack, A., and U. Schumann, 1993: Numerical simulation of turbulent convective flow over wavy terrain. *Bound.-Layer Meteor.,* **65,** 323–355.

Doyle, J. D., and D. R. Durran, 2002: The dynamics of mountain-wave-induced rotors. *J. Atmos. Sci.,* **59,** 186–201.

Durran, D. R., 1986: Another look at downslope windstorms. Part I: The development of analogs to supercritical flow in an infinitely deep, continuously stratified fluid. *J. Atmos. Sci.,* **43,** 2527–2543.

Farmer, D. M., and L. Armi, 1999: Stratified flow over topography: The role of small scale entrainment and mixing in flow reestablishment. *Proc. Roy. Soc. London,* **A455,** 3221–3258.

Gallus, W. A., and J. B. Klemp, 2000: Behavior of flow over step orography. *Mon. Wea. Rev.,* **128,** 1153–1176.

Gong, W., P. A. Taylor, and A. Dörnbrack, 1996: Turbulent boundary-layer flow over fixed aerodynamically rough two-dimensional sinusoidal waves. *J. Fluid Mech.,* **312,** 1–37.

Harlow, F. H., and J. E. Welch, 1965: Numerical calculation of time-dependent viscous incompressible flow of fluid with free surface. *Phys. Fluids,* **8,** 2182–2189.

Kim, Y.-J., and A. Arakawa, 1995: Improvement of orographic gravity wave parameterization using a mesoscale gravity wave model. *J. Atmos. Sci.,* **52,** 1875–1902.

Krettenauer, K., and U. Schumann, 1992: Numerical simulation of turbulent convection over wavy terrain. *J. Fluid Mech.,* **237,** 261–299.

Kundu, P. K., 1990: *Fluid Mechanics.* Academic Press, 638 pp.

Lamb, K. G., 1994: Numerical simulations of stratified inviscid flow over a smooth obstacle. *J. Fluid Mech.,* **260,** 1–22.

Long, R. R., 1955: Some aspects of the flow of stratified fluids. III. Continuous density gradients. *Tellus,* **7,** 341–357.

Nash, J. D., and J. N. Moum, 2001: Internal hydraulic flows on the continental shelf: High drag states over a small bank. *J. Geophys. Res.,* **106,** 4593–4612.

Peltier, W. R., and T. L. Clark, 1979: The evolution and stability of finite-amplitude mountain waves. Part II: Surface wave drag and severe downslope winds. *J. Atmos. Sci.,* **36,** 1498–1529.

Skyllingstad, E. D., W. D. Smyth, J. N. Moum, and H. Wijesekera, 1999: Resonant wind-driven mixing in the ocean boundary layer. *J. Phys. Oceanogr.,* **30,** 1866–1890.

Smith, R. B., 1985: On severe downslope winds. *J. Atmos. Sci.,* **42,** 2597–2603.

Smolarkiewicz, P. K., and L. G. Margolin, 1994: Variational solver for elliptic problems in atmospheric flows. *Appl. Math. Comput. Sci.,* **4,** 527–551.

Steppler, J., H.-W. Bitzer, M. Minotte, and L. Bonaventura, 2002: Nonhydrostatic atmospheric modeling using a *z*-coordinate representation. *Mon. Wea. Rev.,* **130,** 2143–2149.

Tripoli, G. J., 1992: A nonhydrostatic mesoscale model designed to simulate scale interaction. *Mon. Wea. Rev.,* **120,** 1342–1359.

Turner, J. S., 1973: *Buoyancy Effects in Fluids.* Cambridge University Press, 368 pp.

Uchida, T., and Y. Ohya, 2001: Numerical study of stably stratified flows over a two-dimensional hill in a channel of finite depth. *Fluid Dyn. Res.,* **29,** 227–250.

Winters, K. B., and E. A. D'Asaro, 1994: Three-dimensional wave instability near a critical level. *J. Fluid Mech.,* **272,** 255–284.

Wu, X., and K. D. Squires, 1998: Numerical investigation of the turbulent boundary layer over a bump. *J. Fluid Mech.,* **362,** 229–271.

Xue, M., K. K. Droegemeier, V. Wang, A. Shapiro, and K. Brewster, 1995: *Advanced Regional Prediction System User's Guide.* University of Oklahoma, 380 pp.